Published in final edited form as:

Adv Funct Mater. 2020 November 11; 30(46): . doi:10.1002/adfm.202003740.

Bioprinted Injectable Hierarchically Porous Gelatin Methacryloyl Hydrogel Constructs with Shape-Memory Properties

Guoliang Ying,
Division of Engineering in Medicine, Department of Medicine, Brigham and Women's Hospital, Harvard Medical School, Cambridge, MA 02139, USA

Nan Jiang,
School of Engineering and Applied Sciences, Harvard University, Cambridge, MA 02138, USA

Carolina Parra,
Division of Engineering in Medicine, Department of Medicine, Brigham and Women's Hospital, Harvard Medical School, Cambridge, MA 02139, USA

Guosheng Tang,
Division of Engineering in Medicine, Department of Medicine, Brigham and Women's Hospital, Harvard Medical School, Cambridge, MA 02139, USA

Jingyi Zhang,
Division of Engineering in Medicine, Department of Medicine, Brigham and Women's Hospital, Harvard Medical School, Cambridge, MA 02139, USA; State Key Laboratory of Bioelectronics, School of Biological Science and Medical Engineering, Southeast University, Nanjing 210096, China

Hongjun Wang,
Department of Surgery-Transplant and Holland Regenerative Medicine Program University of Nebraska Medical Center, Omaha, NE 68198, USA

Shixuan Chen,
Department of Surgery-Transplant and Holland Regenerative Medicine Program University of Nebraska Medical Center, Omaha, NE 68198, USA

Ning-Ping Huang,
State Key Laboratory of Bioelectronics, School of Biological Science and Medical Engineering, Southeast University, Nanjing 210096, China

Jingwei Xie,
Department of Surgery-Transplant and Holland Regenerative Medicine Program University of Nebraska Medical Center, Omaha, NE 68198, USA

Yu Shrike Zhang
Division of Engineering in Medicine, Department of Medicine, Brigham and Women's Hospital, Harvard Medical School, Cambridge, MA 02139, USA

---

yszhang@research.bwh.harvard.edu.

Supporting Information
Supporting Information is available from the Wiley Online Library or from the author.

Abstract

Direct injection of cell-laden hydrogels shows high potentials in tissue regeneration for translational therapy. The traditional cell-laden hydrogels are often used as bulk space fillers to tissue defects after injection, likely limiting their structural controllability. On the other hand, patterned cell-laden hydrogel constructs often necessitate invasive surgical procedures. To overcome these problems, herein, we report a unique strategy for encapsulating living human cells in a pore-forming gelatin methacryloyl (GelMA)-based bioink to ultimately produce injectable hierarchically macro-micro-nanoporous cell-laden GelMA hydrogel constructs through three-dimensional (3D) extrusion bioprinting. The hydrogel constructs can be fabricated into various shapes and sizes that are defect-specific. Due to the hierarchically macro-micro-nanoporous structures, the cell-laden hydrogel constructs can readily recover to their original shapes, and sustain high cell viability, proliferation, spreading, and differentiation after compression and injection. Besides, *in vivo* studies further reveal that the hydrogel constructs can integrate well with the surrounding host tissues. These findings suggest that our unique 3D-bioprinted pore-forming GelMA hydrogel constructs are promising candidates for applications in minimally invasive tissue regeneration and cell therapy.

Graphical Abstract

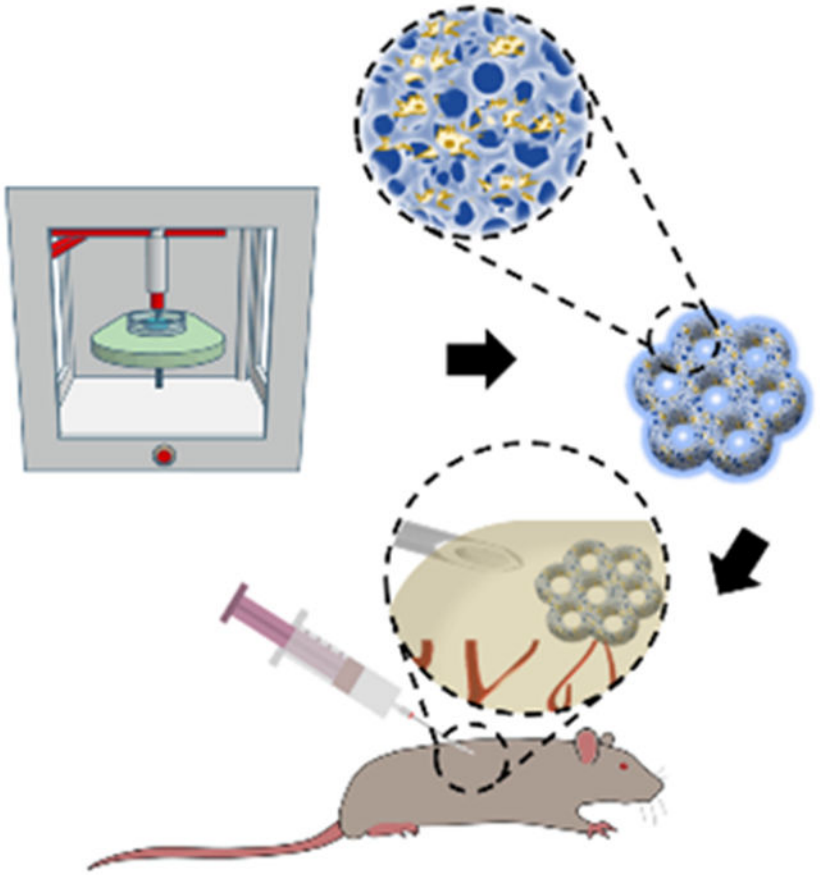

An aqueous two-phase emulsion bioink is used to fabricate hierarchically macro-micro-nanoporous cell-laden GelMA hydrogel constructs via three-dimensional extrusion bioprinting. A

variety of shapes and sizes of the hydrogel constructs can be minimally invasively injected, and readily shape-recovered to fill irregular defects. The encapsulated cells maintain their viabilities, proliferation, spreading, and differentiation after injection.

Keywords

Injectable cell-laden hydrogel; 3D bioprinting; pore-forming hydrogel; shape-memory hydrogel; minimally invasive tissue repair

1. Introduction

Minimally invasive injection provides an enabling platform to deliver biomaterial implants to the defect sites of injured tissues for wound repairing and tissue regeneration.[1] It overcomes limitations of clinical implantation, which not only possesses high risks of infection or inflammation,[1a] but also requires trained clinicians for sophisticated surgical operations, and oftentimes involves low patient compliance. Nevertheless, directly injecting therapeutic cells into the defect sites is subjected to low retention and engraftment efficacies. Due to their high water contents and tissue-like mechanical properties, hydrogels laden with therapeutic cells as biomimetic living tissues have been considered as a class of favorable vehicles serving the purpose of minimally invasive injection through percutaneous needles or catheters.[2] Cell-laden precursors in a liquid phase could readily fill the defects and subsequently form hydrogels *in situ*.[3] Yet, the post-polymerization typically involves difficulties to precisely control the gel location, gelation time, mechanical properties, and fine structures *in vivo*.[4] Traditional cell-laden hydrogels can also be synthetized *in vitro*; however, invasive operational procedures are frequently required for subsequent implantation.[5] On the other hand, these hydrogels are also usually bulky and dense, which may easily clog the needles during the injections or crush after injections.[6]

To ensure that the cell-laden hydrogel constructs can be properly utilized to repair the damaged tissues after injection, the defect shapes should be promptly accommodated by the polymerized hydrogel constructs. Microgels, or the microscale cell-laden hydrogels, have been introduced to allow convenient injection and filling of defects *via* self-assembly *in vivo*.[7] Nevertheless, the stability and controllability of these injectable microgels within relatively large defects or wounds remain a challenge, due to the weak interactions between each assembled microgel. On the contrary, an ideal injectable cell-laden gel with a defined structure must maintain its original shape and structural integrity, and also be sustainable to cell survival and functions post-injection, since both of the encapsulated cells and the hydrogel are subjected to external shear forces or compressions during the process of injection that may easily deform the structure of the hydrogels and cause cell death.

To this end, a hydrogel featuring an interconnected micro-nanoporous structure could store and release elastic energy that in turn supports its recovery to the original shape after the removal of external stress.[8] Moreover, the interconnected micropores not only allow efficient exchanges of nutrients and metabolites with surrounding microenvironments for the laden cells but also provide enough spaces for tissue ingrowth or cell delivery. Yet, standard hydrogel constructs only possess the intrinsic nanopores formed by crosslinked polymer chains;[9] these nanoscale pores are usually either insufficient for shape recovery or limited in promoting cellular activities. Cryogels as a class of highly micro-nanoporous cell-laden hydrogels have been created by a cryo-gelation method.[8b, 10] Due to the micro-nanoporous structures, the cryogels are easily compressed and injected through a surgical needle, and readily recover to their original shapes afterwards. However, this approach requires extremely low temperatures that are not applicable to encapsulation of living cells during the fabrication. As a result, cells can only be post-seeded into the cryogels. Micelle-templating methods using Pluronics also provide a possibility to produce microscale pores within hydrogel constructs under mild conditions.[11] However, due to the limitation of the micelle sizes, this approach has been difficult to fabricate cell-laden hydrogel constructs with large pores to achieve shape recovery. Therefore, a strategy that enables generation of micro-nanoporous cell-laden hydrogel constructs with controllable geometries under a mild condition is urgently required for future personalized, minimally invasive tissue regeneration.

Three-dimensional (3D) bioprinting provides a versatile platform to precisely produce volumetric hydrogel constructs with sophisticated architectures in a spatially controllable manner.[12] The 3D-bioprinted cell-laden hydrogels could therefore intimately meet the needs for various customizable shapes at the macroscale for tissue repair.[13] Although 3D bioprinting has been widely used to engineer macro-nanoporous cell-laden hydrogels with a variety of defined shapes, creating micro-nanoporous-structured cell-laden hydrogels that simultaneously possess excellent injectability and shape-recovery property post-injection remains an unmet need. Recently, we have developed an aqueous two-phase emulsion bioink that could allow facile fabrication of micro-nanoporous cell-laden hydrogels with defined shapes.[14] The interconnected micropores in the hydrogels facilitated cell growth, proliferation, and migration.

Here, we report the unique potential of the 3D-bioprinted cell-laden hierarchically macro-micro-nanoporous hydrogel constructs with customizable shapes to be injected and shape-recovered through conventional percutaneous needles, for minimally invasive therapy. Gelatin methacryloyl (GelMA), possessing advantages of on-demand photocrosslinkability, tunable physicochemical properties, and intrinsic bioactivity was used as the hydrogel material.[15] GelMA as a derivative of gelatin, possesses temperature-sensitive properties, which could induce the formation of a GelMA physical gel that enables a direct extrusion bioprinting of macro-nanoporous GelMA hydrogels.[15] Apart from their printability, the GelMA solution could blend with the PEO aqueous solution to form a cytocompatible aqueous two-phase emulsion bioink that allows generation of interconnected micropores within cell-laden hydrogel constructs after photo-polymerization. Of note, poly(ethylene oxide) (PEO), similar to the poly(ethylene glycol) (PEG) at small molecular weights, is also a nontoxic and biocompatible polymer that has been widely utilized as a medical material.[16] To benchmark the hierarchically porous GelMA hydrogel constructs as a new class of injectable scaffolds that enable irregular defects repair, the immediate shape recovery of the hydrogel constructs post-compression and post-injection, as well as maintained cell viability and morphological and functional characteristics were systematically investigated *in vitro* and *in vivo*.

2. Results and Discussions

2.1 Synthesis of Hierarchically Macro-micro-nanoporous Cell-laden Hydrogel Constructs

A schematic overview presenting the fabrication process of the injectable 3D-bioprinted cell-laden hydrogel constructs featuring interconnected hierarchically macro-micro-nanopores is shown in Figure 1. To produce the interconnected micropores, an aqueous two-phase bioink was prepared by mixing a blend of GelMA pre-gel solution containing cells with a PEO solution at an optimized volume ratio under room temperature (Fig. 1a). An extrusion-based 3D bioprinter was used to build defined 3D architectures, which were subsequently photocrosslinked to produce cell-laden hydrogel constructs (Fig. 1b). The hydrogel constructs could then be conveniently injected *in vivo*, *ex vivo*, or *in vivo* using a commercial percutaneous needle (Fig. 1c).

Specifically, the macroporous structures were fabricated by direct extrusion 3D-bioprinting (Fig. 1d-i). The PEO droplets in the GelMA hydrogel network were removed by immersing in phosphate-buffered saline (PBS) or cell culture medium to generate interconnected micropores (Fig. 1d-ii). The GelMA hydrogel network itself further contains the intrinsic nanopores to supply the constructs with mechanical strength (Fig. 1d-iii). These nanopores are indicative of interchain distances that might be formed by the crosslinked polymer chains within the GelMA hydrogel.[17]

2.2 Characterizations of the Hydrogel Constructs

The 3D-bioprinted hydrogel constructs with different spatial shapes were visualized in both fluorescence and bright-field photographs (Figs. 2a and S1, and Mov. S1). The interconnected micropores within the GelMA hydrogel constructs with an average pore size of 60 μm are shown in Figure 2b. To control the porosity of the hydrogel constructs, the PEO volume fraction was varied from 50% to 10% in the aqueous two-phase bioink. The hydrogel constructs with different pore sizes are shown in Figure 2c. The hydrogel networks conjugated with rhodamine B emitted red fluorescence, while dark areas indicated the micropores (Fig. 2c-i). The hierarchically porous hydrogel constructs and the standard hydrogel constructs were further freeze-dried and characterized by a scanning electron microscope (SEM) (Fig. 2c-ii and Fig. S3). The porosities of the hydrogel constructs in SEM micrographs were comparable to those suggested by their respective fluorescence micrographs, demonstrating the high stability of the micro-nanoporous structure of the hydrogel constructs. With decreasing PEO volume fraction from 50% to 10%, the average micropore size of the hydrogel constructs was reduced from 53±9 μm to 18±5 μm. Moreover, as the mixing time was prolonged from 5 s to 20 s, the average pore size decreased by 50% (Fig. S4), confirming that the porosity could be conveniently adjusted by tuning the PEO volume fraction and mixing time.

Since the hierarchically micro-nanoporous structure of the hydrogel constructs was produced from the aqueous two-phase bioink, the rheological properties of the bioinks were investigated for a better understanding of their printability.[18] As the rheology of the GelMA pre-gel solution can be readily controlled by temperature,[19] the rheological properties of the bioinks were studied by adjusting the PEO volume fraction and in relationship to temperature. The measurement was performed at a constant shear rate at 50 s^{-1} with decreasing temperatures from 36 °C to 6 °C at a cooling rate of 1 °C min^{-1} (Fig. 2e). It was observed that the viscosities of all the bioink samples were decreased with the increment of temperature from 6 °C to 25 °C. As the PEO volume fraction was increased from 0% to 50%, the effect of the temperature on the viscosity of the bioink reduced 3.5-fold. The viscosity of the bioink kept constantly low at 0 Pa·s when the temperature was above 25 °C. As such, both the temperature and the PEO volume fraction were critical to determining the viscosity of the bioink with a defined formulation. To maintain the stability of the porous structure, the 3D bioprinting process was performed at 15 °C at a nozzle moving speed of 360 mm min^{-1}, where the extrusion was controlled by gas pressure (20 psi) to match the extruding speed and bioprinting speed.

The effect of the micro-nanoporous structure on the mechanical properties of the hydrogel constructs with different formulations was also investigated using a mechanical analyzer in the unconfined compression mode. The hydrogel constructs were axially compressed in PBS at room temperature. Upon unconfined compression, the hydrogel constructs presented a non-linear stress-strain response (Fig. 2f). Standard hydrogel constructs gave Young's modulus of 23 kPa (Fig. S5). In comparison, as the PEO volume fraction was increased to 50% (average pore size of 53 μm), the hydrogel constructs showed a dramatic reduction in Young's modulus to 1 kPa. The stress-strain curves conveyed that the micro-nanoporous hydrogel constructs had a higher mechanical strain under the same compression stress compared to the standard hydrogel constructs before fracture. For example, when the hydrogel constructs were strained by 30% without damaging the structures, the applied compression stress on the standard hydrogel constructs was 13 kPa, while the stresses on the micro-nanoporous hydrogel constructs were below 1.5 kPa. This observation suggested that the micro-nanoporous hydrogel constructs had the potentials for allowing minimally invasive injection. The subsequent reversibility test of the micro-nanoporous hydrogel constructs is presented in Figure 2g. Comparing the micro-nanoporous hydrogel constructs before and after the compression cycle, the strain-stress curves remained similar, indicating that the porous hydrogel constructs could readily recover from the mechanical compression.

2.3 Compressibility of the Hydrogel Constructs

As shape recovery is a key factor in determining the injectability of hydrogel constructs, further studies on the shape-memory properties were conducted. The hydrogel constructs were sandwiched between two glass pressure pads and axially compressed under a constant mechanical load of 1 N with the strain of 60% at room temperature (Fig. 3a, and Movs. S2 and S3). Examination of the standard hydrogel constructs in the compression test revealed that the shape was destructed after a single-time compression (Mov. S2). Fluorescence micrographs further proved that the standard hydrogel constructs failed to recover and maintain the structural integrity after compression (Fig. 3b), indicating a poor shape-memory property of the standard hydrogel constructs. In comparison, the micro-nanoporous hydrogel constructs exhibited a high reversible response to external compressions (Mov. S3). When compressed, the porous hydrogel constructs expanded leading to increments of both diameter (Fig. 3c) and average pore size in the lateral direction (Fig. 3d). After the stress was removed, the hydrogel constructs quickly recovered to their original shape at a relaxed state without structure damage, which was consistent with the result of the reversibility test illustrated in Figure 2g. Even after 50 cycles of compression test, the diameter and the pore size remained similar to those under the original relaxed state. Thus, the 3D-bioprintable micro-nanoporous hydrogel constructs were not affected by the mechanical compression at the strain level assessed.

2.4 Injectability of the Hydrogel Constructs

The ability of the 3D-bioprinted hierarchically porous hydrogel constructs to flow through commonly used-gauge percutaneous needles, and subsequently re-obtain their original shape integrity post-injection, was examined. Subject to shear stress and physical confinement during flowing through the percutaneous needles, the hydrogel constructs would experience a body force similar to the applied compression, which could cause their collapse. The 3D-bioprinted hierarchically macro-micro-nanoporous hydrogel constructs with different degrees of methacryloyl substitution (low, medium, and high) were suspended in 2 mL of PBS, and then syringe-injected employing different gauges of the percutaneous needles (10-18G) (Fig. 4a and Table S1). The obvious change in passage efficiency of the injected hydrogel constructs was caused by the differences of the inner diameters of the syringe needles and irreversible collapse of the micropores within the hydrogel network. The 3D-bioprinted macropores enabled the standard hydrogel constructs to readily pass through 10G and 12G needles. However, their shapes still collapsed after injection through thinner needles (*e.g.*, 14-18G) (Fig. S6). On the contrary, when the micropores were further introduced, the hierarchically macro-micro-nanoporous hydrogel constructs of the same size/architecture could conveniently pass through 10-16G needles (inner diameters: 2.96-1.32 mm) and rapidly recover to their original shapes. In addition, in comparison with the micro-nanoporous hydrogels (Fig. S7), the macro-micro-nanoporous hydrogel constructs showed improved shape integrity after injection. These comparisons demonstrated that the shape-memory property was mainly contributed by primarily the interconnected micropores but also to a level the macropores within the hydrogel constructs. To evaluate the effect of the degree of methacryloyl substitution and PEO volume fraction on passage efficiency, the hydrogel constructs with different formulations were analyzed using a 14G needle (Fig. 4b and Movs. S4-S7). It was observed that when the PEO volume fraction was kept constant at 50%, the passage efficiency was increased from 60% to 96% as the degree of methacryloyl substitution was elevated from low to high (Fig. 4b and Table S2). Fluorescence micrographs further visualized the structural changes of the *in vitro*-injected hydrogel constructs (Fig. 4c and 4d), which were consistent with quantitative results shown in Figure 4a and 4b.

To assess whether the 3D-bioprinted micro-nanoporous hydrogel constructs could maintain injectability and shape-memory property to conform to irregular defects in biological tissues, *ex vivo* tests were conducted by injecting the micro-nanoporous hydrogel constructs of different patterns into the defects in porcine tissues using a 14G needle (Fig. 4e and Mov. S8). Extrusion 3D bioprinting was again used to fabricate the micro-nanoporous hydrogel constructs with matching sizes and patterns as the defects. After syringe injection, the hydrogel constructs with different patterns were observed to promptly recover to the original shapes, which precisely fit the defects in the porcine tissues (Fig. 4f). The results evidenced the injectability and shape-memory property of the 3D-bioprinted micro-nanoporous hydrogel constructs in an *ex vivo* setting.

2.5 Biological Characterizations of the Hydrogel Constructs

The physiological characteristics of laden cells within the 3D-bioprinted hydrogel constructs are essential for *in vivo* injection to achieve tissue repair. As such, the viability, spreading, proliferation, and differentiation of the cells within the 3D-bioprinted hierarchically porous hydrogel constructs after compression and injection were investigated. Human mesenchymal stem cells (hMSCs) are classified as multipotent progenitor cells that can be directed to differentiate into specific lineages to promote the regeneration of different tissues.[20] Normal hMSCs possess the capability to naturally migrate to defects of tissues to accelerate the process of tissue repair.[21] The compression and injection tests of the 3D-bioprinted hydrogel constructs were performed under the same conditions as those of the tests shown in Figures 3 and 4. The 3D-bioprinted hMSC-laden hydrogel constructs were subsequently cultured and the viabilities of hMSCs were evaluated by the Live/Dead assay (Figs. 5a and S8). The live cells were stained in green, while dead in red. It was shown that aggregated cells were rarely observed before and after compression and injection, demonstrating the good distribution of the hMSCs in the hydrogel constructs before and after these procedures. Comparing the samples with/without compression, the hMSCs maintained similar viabilities on Days 1, 3, and 7 (Fig. 5a and 5b), indicating that mechanical compression did not noticeably alter cell viability. Similar results could be acquired from the injection test, where the 3D-bioprinted hierarchically porous hMSC-laden hydrogel constructs were injected under the same conditions as those in Figure 4a. Proliferation evaluations further presented that the mechanical compression or needle injection did not affect the proliferation rate of the encapsulated hMSCs (Fig. 5c). Moreover, both of cell viability and proliferation data confirmed that the encapsulated hMSCs were most likely not pushed out of the hydrogel constructs during the compression or injection (Fig. 5a-c).

The effect of compression and injection on hMSC spreading was then investigated by measuring spreading hMSC areas within the hydrogel constructs (Fig. 5d). The area of spreading hMSCs was calculated to be 5224±735 μm^2, indicating a well-spreading behavior of the cells in the hierarchically porous hydrogel constructs as compared with the cells in the standard hydrogel constructs at 841± 61 μm^2 of the spreading area (Fig. S9, and Movs. S9 and S10). On Day 7 after compression or injection, the cell areas were measured to be 5547±1141 μm^2 or 5625±871 μm^2, respectively, which demonstrated that these procedures did not affect cell spreading. Taken together, neither the compression nor injection process affected the viability, proliferation, and spreading of hMSCs within the 3D-bioprinted hierarchically porous hydrogel constructs, making them potentially amenable to injection and delivery in the presence of cells.

To investigate the effect of compression or injection on the differentiating capabilities of hMSCs within the hierarchically porous hydrogel constructs, adipogenic and osteogenic differentiation of the encapsulated hMSCs, as well as associated staining were conducted (Fig. 6). Adipogenesis was induced for up to 3 weeks,[22] and Oil red O staining was utilized to characterize the formation of oil drops. The stained area was 4-fold larger in the micro-nanoporous hydrogel constructs than in the standard hydrogel constructs after a 3-week of adipogenic differentiation (Figs. 6a-ii and S10a). The results in Figure 6a also evidenced that the compression and injection did not affect the adipogenesis process. Peroxisome proliferator-activated receptor gamma (PPARγ) immunostaining demonstrated that no obvious change in the stained areas was observed or quantified between the control samples (porous hydrogel constructs without compression or injection) and those compressed or injected (Fig. 6b), indicating that the compression or injection did not affect hMSC adipogenesis. Furthermore, PPARγ expression levels were both 5-fold higher than the respective counterparts in standard hydrogel constructs after 1-week and 2-week differentiation (Figs. 6b-ii and 6d-ii, and S11). At 3 weeks, the micro-nanoporous hydrogel constructs encouraged an up to 21-fold increase in the PPARγ-stained area over the standard hydrogel constructs.

For osteogenesis differentiation, hMSC-laden hydrogel constructs were cultured in the osteogenic differentiation medium for 3 weeks. After staining with Alizarin Red S, the mineralized nodules deposited by the hMSCs exhibited a 2-fold larger amount in the micro-nanoporous hydrogel constructs than in standard hydrogel constructs (Fig. S10b and S10c). Similar results were presented between the control samples and compressed/injected samples (Fig. 6c-i and 6c-ii). The deposited calcium mineral was also observed on the cell surface and in the surrounding regions within the micro-nanoporous hydrogel construct. Spectrometric analyses of Alizarin Red S staining post-osteogenic differentiation of the hMSC-laden hydrogel constructs were carried out. As compared with standard hydrogel constructs, the detected average optical density was 2.3-fold higher in the porous hydrogel constructs (Fig. S10d). There were no significant differences in optical densities after compression/injection. A single differentiated cell is clearly shown in the SEM image (Fig. 6c-iii). Runt-related transcription factor 2 (RUNX2, 1 week) and osteocalcin (2-3 weeks) immunostaining results further demonstrated that a large amount of the stained bone lineage (74%±13%) was observed in the micro-nanoporous hydrogel constructs, while only a few stained cells (7.6%±2.2%) were present in the standard hydrogel constructs (Figs. 6d-ii and S11). This result indicated that the produced hierarchically porous hydrogel constructs facilitated osteogenesis as compared with their counterparts. Moreover, hMSCs undergoing compression or injection exhibited similar behaviors as compared with control samples.

Taken together, the retained and promoted adipogenic and osteogenic differentiation potentials of the hMSCs within the 3D-bioprinted micro-nanoporous hydrogel constructs were probably because that the micropores within the polymeric networks provide enough space for cell proliferation, migration, and differentiation. Importantly, the characteristics of adipogenesis and osteogenesis were not affected after compression or injection. The maintained structural and functional characteristics of hMSCs after applying external mechanical forces were presumably also due to the micropores, which allowed sufficient spaces to minimize the impact on living cells when the volumes of the constructs were reduced.

2.6 *In vivo* Evaluation of the Hydrogel Constructs

To evaluate the ability of the hydrogel constructs to be delivered and become fully integrated into the defect areas without the risk of displacement during regeneration, both the standard and the micro-nanoporous hydrogel constructs were subcutaneously injected in Sprague-Dawley rats and evaluated for tissue ingrowth and degradation up to 2 weeks (Fig. 7a). The implanted hydrogel constructs underwent a reduction in the bulk sizes. Masson's trichrome and hematoxylin and eosin (H&E) staining images revealed mild inflammation after implantation including the presence of macrophages, multinucleated giant cells, fibroblasts, and collagen, as well as the biodegradability of the hydrogel constructs within the subcutaneous tissue pockets (Fig. 7b and 7c). It was further observed that a large portion of the standard hydrogel constructs was detached from the subcutaneous tissues. On the contrary, the porous hydrogel constructs were sufficiently flexible to fill the complex shapes of lacunae and were in intimate contact with the surrounding tissues, which is essential for tissue repairing. After a 2-week post-implantation period, the tissue ingrowth of the porous hydrogel constructs was quantified to be over 50%, while that of the counterparts was only at less than 2% (Fig. 7d). At 4 weeks, the hydrogels were completely degraded and could not be found anymore. The significant differences in tissue ingrowth between standard hydrogel and porous hydrogel were mainly attributed to the interconnected micropores within the porous hydrogel constructs that provided enough spaces for tissue in-growth. The standard hydrogels having only tight nanopores might instead, limit tissue infiltration. This study demonstrates the excellent malleability and shape-conformability of the micro-nanoporous hydrogel constructs.

Moreover, the biodegradability of the hydrogel constructs was observed. It was revealed that the micro-nanoporous structure was maintained after *in vivo* injection. As shown in the 1- and 2-week histology images, the average size of the lacunae (white areas) increased as degradation of the hydrogel constructs proceeded. The micro-nanoporous hydrogel constructs showed a significantly higher degradation rate than the standard constructs at both time points (Fig. 7e). The remaining areas of porous hydrogel constructs at the implantation sites were calculated to be 1.5-fold and 2-fold smaller than those of the counterparts of the standard hydrogels after 1-week and 2-week of implantation, respectively (Fig. 7f). Taken together, the histological assessment confirmed that the 3D-bioprinted micro-nanoporous hydrogel constructs could effectively seal the defects of the tissue and strongly attach to the defect sites after *in vivo* application. These micro-nanoporous hydrogel constructs were evidenced as a potential enabling platform to support minimally invasive delivery and subsequent repair of the defects *in vivo*.

3. Conclusions

In summary, the 3D-bioprinted cell-laden hierarchically porous GelMA hydrogel constructs have been developed with their favorable capacities demonstrated. The micropores not only greatly improved the compressibility and injectability of the cell-laden hydrogel constructs, but also allowed for hMSC proliferation, migration, and differentiation. Moreover, the injectable hydrogel constructs with the shape-memory property were biodegradable and could enhance tissue ingrowth *in vivo*. This new class of injectable 3D-bioprinted cell-laden porous hydrogels represents a promising vehicle for minimally invasive injection and wound repair.

3D bioprinting has provided a versatile platform to produce desired shapes of hydrogel constructs that could fit the defects. Apart from their tunable mechanical properties, these hydrogel constructs showed superior injectability and shape-memory property both *in vitro*, *ex vivo*, and *in vivo*, primarily due to the interconnected micro-nanoporous structure of the hydrogel constructs. Moreover, the biological studies revealed that the hydrogel constructs maintained their original structural and functional characteristics post-compression and post-injection.

A key feature of the biodegradable GelMA hydrogel constructs is to provide temporary structural integrity until the biological tissues are healed or regenerated. While the sizes and shapes of the constructs should be maintained, it requires the biodegradation rates and mechanical properties of the hydrogel constructs to be precisely controlled. Since the GelMA hydrogels used as constructs in this work are originally derived from biological tissues, they suffer from a relatively rapid degradation rate *in vivo*. Increasing the degree of methacryloyl substitution would partially decrease the degradation rate. Other possible strategies to prolong the degradation time could be achieved by incorporating other biocompatible components.[23] The higher mechanical property could be further accessed by incorporating bioinorganic materials (such as hydroxyapatite[24]) as needed.

Since our 3D-bioprinted hierarchically macro-micro-nanoporous cell-laden hydrogel constructs showed the ability to conform to the tissue sites *in vivo*, various types of cells have potentials to be encapsulated within the constructs for the regeneration of different tissues, such as the neuronal tissue,[25] bone tissue,[26] skin tissue,[27] and vascular networks,[28] among others. Therefore, these unique hydrogel constructs are believed to possess a remarkable potential to be utilized as injectable implants that can support tissue repairing *in vivo* for regenerative therapy.

4. Experimental Section

Materials:

Cryopreserved hMSCs were purchased from Lonza. Gelatin (derived from porcine skin, Type A, ~300 g Bloom, average M_w=90,000 Da), methacrylic anhydride, PEO (average M_w=300,000), rhodamine B, PBS, dimethyl sulfoxide (DMSO), paraformaldehyde, Dulbecco’s Modified Eagle Medium (DMEM), fetal bovine serum (FBS), penicillin-streptomycin (P/S), trypsin-EDTA, formalin, dexamethasone, indomethacin, ethanol, glutaraldehyde solution, L-ascorbic acid, insulin, acepromazine maleate, ketamine hydrochloride, β-glycerol phosphate, (+,-)-thiopental sodium, formaldehyde solution, H&E staining kit, propidium iodide, and Masson’s trichrome stain kit were purchased from Sigma-Aldrich. LIVE/DEAD™ viability/Cytotoxicity Kit, PrestoBlue® cell viability reagent, Alexa 488-phalloidin, and dialysis membranes (M_w cut-off=12,000-14,000 Da) were purchased from ThermoFisher. Lithium phenyl -(2,4,6-trimethylbenzoyl) phosphinate (LAP, the photoinitiator) and printheads (26G needles, 0.25” in length) were purchased from Allevi. Sterilized syringe filters (0.22 μm in pore size) were purchased from VWR

International. 10-18G needles were purchased from McMaster-Carr. Fluorescent colors were purchased from Create Colors. Anti-osteocalcin antibody [OC4-30] (ab13418) and goat anti-mouse IgG H&L (Alexa Fluor® 488) (ab150113) were purchased from Abcam. Anti-PPARγ antibody (E-8) was purchased from Santa Cruz Biotechnology.

hMSCs culture:

For standard cell culture, hMSCs were maintained in a DMEM supplemented with 10 vol% FBS and 1 vol% P/S at 37°C and 5 vol% CO_2. For hMSC differentiation, the standard culture medium was replaced with pure DMEM supplemented with 20 vol% FBS and 1 vol % P/S priority to differentiation. For adipogenesis, the hMSCs were maintained in a 4.5 g L^{-1} of D-glucose DMEM containing dexamethasone (1 μmol L^{-1}), insulin (5 μg mL^{-1}), and indomethacin (50 μmol L^{-1}).[22] For osteogenesis, hMSCs were cultured in a 1 g L^{-1} of D-glucose DMEM containing β-glycerol phosphate (10 mmol L^{-1}), L-ascorbic acid (300 μmol L^{-1}), and dexamethasone (100 nmol L^{-1}).[22]

3D bioprinting of cell-laden hierarchically porous hydrogel constructs:

GelMA was first synthesized according to our established protocol,[14] at a high methacryloyl substitution degree (71.6±0.5%). When cell encapsulation was needed, hMSCs were trypsinized and mixed with the GelMA pre-gel solution (10%, containing 0.5% LAP) at a cell concentration of 5×10^6. PEO solution was prepared by dissolving PEO powder in the LAP solution (0.5 wt% in PBS) at a concentration of 1.6%. The bioink was prepared by mixing the PEO solution with the pre-gel solution. The 3D-bioprinted hydrogel constructs were fabricated by extrusion bioprinting using a bioprinter (Allevi 2). Briefly, the prepared bioink was transferred to a 10-mL syringe and cooled down to 4 °C for 20 min. The bioprinting process was conducted at 15 °C at a speed of 360 mm min^{-1}, which was controlled by gas pressure at 20 PSI. Finally, the hydrogel constructs were crosslinked with UV exposure (0.5 W cm^{-2}, 15 s). The standard GelMA hydrogel was prepared by dissolving the freeze-dried GelMA foam and LAP (0.5 wt%) in PBS and crosslinking under the UV light (0.5 W cm^{-2} for 15 s) to obtain a final GelMA concentration at 10 w/v%.

Measurements of structural, mechanical, and rheological properties:

To observe the microstructure of the hydrogel constructs, the 3D-bioprinted hydrogel constructs were conjugated with rhodamine B, and observed under an inverted fluorescence microscope (Eclipse, Nikon). For SEM (JSM-5600LV, JEOL), the hydrogel constructs were lyophilized and sputter-coated with gold before imaging. The mechanical properties of the hydrogel constructs were measured by using a mechanical testing machine in the compression mode at a working temperature of 24 °C (Instron 5943). The rheological properties of the bioinks were tested by using a rheometer (AR-G2, TA Instruments) equipped with a 40-mm diameter and 2° cone plate, and at a 54-μm plate-to-plate distance.

Evaluation of injectability and shape recovery:

For the compression test, a 3D-bioprinted hydrogel construct was placed between two pieces of flat substrates. A 1-N force was exerted on the hydrogel constructs and maintained for 10 s. For the injection test, the 3D-bioprinted hydrogel constructs were injected through syringe needles of different gauges, spanning across 10-18G. Shape integrity was evaluated by photographing after compression and injection. For *ex vivo* test, a porcine tissue was cropped with a biopsy punch to create defects with different shapes. A 14G needle was pierced through the tissues and the corresponding hydrogel constructs were then injected into the cropped defects at room temperature.

Evaluation of cell viability and proliferation:

Viability of hMSCs within the hydrogel constructs was investigated by a Live/Dead assay. Briefly, the LIVE/DEAD™ Viability/Cytotoxicity Kit was diluted with PBS to final concentrations of calcein AM at 0.5 μL mL^{-1} and ethidium homodimer-1 at 2 μL mL^{-1}. The hMSC-laden constructs were incubated with the working probe solution (~300 μL) at 37 °C for 25 min. Fluorescence micrographs were captured by using the inverted fluorescence microscope. Live hMSCs were stained in green, while dead cells were stained in red. Quantitative analysis of hMSC viability was performed by counting live and dead cell numbers using ImageJ (National Institutes of Health). hMSC proliferation was evaluated by using a Prestoblue® assay. The hMSC-laden hydrogel constructs were first washed with PBS and individuallyplaced in the wells of a 96-well plate. The PrestoBlue® reagent (20 μL) was added to each well and mixed with culture medium (180 μL) at 37 °C for 4 h. The supernatants were collected and assessed by using a microplate reader (Bio-Tek Instruments).

Evaluation of cell spreading and differentiation:

For cell spreading, the hMSC-laden hydrogel constructs were fixed by a paraformaldehyde solution (3.7 vol% in PBS) and a permeabilization buffer. The constructs were subsequently stained with Alex 488-phalloidin and propidium iodide. For adipogenesis, the anti-PPARγ antibody (E-8) was diluted with PBS at a final concentration of 200 μg L^{-1} and incubated at 4 °C overnight. The stained samples were washed with PBS. The samples were then stained with the secondary antibody. The samples were washed with PBS for observation. For osteogenesis, the samples were stained with a diluted anti-osteocalcin antibody solution at a final concentration of 200 μg L^{-1} at 4 °C overnight. After washing with PBS, the samples were then stained with the secondary antibody. Fluorescence micrographs were captured by using a confocal fluorescence microscope (TCS SP5, Leica). In addition, spectrometric analysis of osteogenic differentiation was performed on the Alizarin Red S staining. The hMSC-laden hydrogel constructs (samples) were individually placed in the wells a 48-microwell plate. 400 μL of 10 vol% acetic acid was added to each well and incubate for 30 min with gentle shaking. The samples were transferred to 1.5-mL microcentrifuge tubes, and vortexed vigorously for 30 s, and subsequently heated to 85 °C for 10 min before transferring to an ice bath for 5 min. 200 μL of the supernatant was collected from each tube into a new microcentrifuge tube after centrifuging for 15 min at 20,000 g. The supernatant (~75 μL) was neutralized with ammonium hydroxide (10 vol%) to reach the pH value within 4.1-4.5. The samples were finally measured using a microplate reader at the absorbance of 405 nm. For SEM, the hMSC-laden hydrogel constructs were treated with glutaraldehyde (2.5 vol%), followed by immersing in a series of ethanol concentrations in deionized water for dehydration. Finally, the samples were freeze-dried and sputter-coated with gold for SEM imaging.

In vivo evaluation of the hydrogel constructs:

Animal experiments were carried out in accordance with the IACUC approved by the University of Nebraska Medical Center (UNMC). 36 male Sprague-Dawley rats (8-10 weeks old) with a mean body weight of 280 g were purchased from Charles Rivers Laboratories. The animals were housed in an AAALAC-accredited animal facility that temperatures (20.0-26.1 °C with a set point of 22.2 °C), humidity (30–70% with a set point of approximately 40%), and light cycles (12/12 h on/off) were monitored continuously. The animals were pair-housed in each cage with unrestricted access to water and food (#8656 Sterilizable 4%, Envigo). The animals were allowed a 3-day acclimation period to facility conditions before study. The animas were randomly divided into two groups (Group A, Group B) of 18 each, with 6 samples per each designed ending time point (1, 2, or 4 weeks). The animals were operated under anesthesia of acepromazine and ketamine under rigorous aseptic conditions. The rats were placed on a circulating warm blanket to maintain their body temperature. An area of 8 × 4-cm^2 on the back of each animal was shaved, and povidone-iodine solution was applied three times on the exposed skin. Subcutaneous pockets were made through 2-cm incisions at the two supraspinal sites on the dorsum. A 3D-bioprinted hydrogel construct was injected into each cavity and the cavity was subsequently sutured. Each rat as such received two same type of implants. Rats were euthanized by CO_2 at 1, 2, and 4 weeks post-implantation. Each explant with the surrounding tissue was gently dissected out of its subcutaneous pocket, and then immersed in formalin for at least 3 days prior to histology analysis. The animals were sacrificed by an overdose of thiopental sodium and the tissue contained hydrogel constructs were retrieved. It should be noted that, at 4 weeks of implantation, no visible hydrogel constructs for both groups could be found any more, and thus we were not able to explant the tissues at this time point for analysis. Otherwise, the samples were fixed in 10 vol% formaldehyde solution for 24 h and rinsed with tap water. Subsequently, the samples were treated with ethanol for dehydration and embedded in paraffin. H&E staining and Masson's trichrome staining were performed on 4-mm-thin cross-sections.

Statistical analysis:

Statistical analyses were performed using unpaired t-tests for comparison of two groups of samples and ANOVA for multiple groups. The statistical significance was determined at $^*p<0.05$ and $^{**}p<0.01$.

Supplementary Material

Refer to Web version on PubMed Central for supplementary material.

Acknowledgements

G.L.Y. and N.J. contributed equally to this work. This work was supported by funding from the National Institutes of Health (K99CA201603, R00CA201603, R21EB025270, R21EB026175, R01EB028143, R01GM134036), the American Heart Association (19TPA34850188), and the Brigham Research Institute.

References

[1]. a)Hilborn J, Wiley Interdisciplinary Reviews: Nanomedicine and Nanobiotechnology 2011, 3, 589 [PubMed: 21780306] b)Cai L, Dewi RE, Heilshorn SC, Adv. Funct. Mater 2015, 25, 1344 [PubMed: 26273242] c)Zeng Y, Zhu L, Han Q, Liu W, Mao X, Li Y, Yu N, Feng S, Fu Q, Wang X, Acta Biomater. 2015, 25, 291. [PubMed: 26234487]

[2]. a)Tseng TC, Tao L, Hsieh FY, Wei Y, Chiu IM, Hsu S. h., Adv. Mater 2015, 27, 3518 [PubMed: 25953204] b)Pupkaite J, Rosenquist J, Hilborn J. n., Samanta A, Biomacromolecules 2019, 20, 3475. [PubMed: 31408340]

[3]. Li B, Wang L, Xu F, Gang X, Demirci U, Wei D, Li Y, Feng Y, Jia D, Zhou Y, Acta Biomater. 2015, 22, 59. [PubMed: 25917845]

[4]. Yu L, Ding J, Chem. Soc. Rev 2008, 37, 1473. [PubMed: 18648673]

[5]. Swartzlander MD, Blakney AK, Amer LD, Hankenson KD, Kyriakides TR, Bryant SJ, Biomaterials 2015, 41, 79. [PubMed: 25522967]

[6]. Piskounova S, Rojas R, Bergman K, Hilborn J, Macromol. Mater. Eng 2011, 296, 944.

[7]. a)Zhao X, Liu S, Yildirimer L, Zhao H, Ding R, Wang H, Cui W, Weitz D, Adv. Funct. Mater 2016, 26, 2809b)Feng Q, Li Q, Wen H, Chen J, Liang M, Huang H, Lan D, Dong H, Cao X, Adv. Funct. Mater 2019, 29, 1906690.

[8]. a)Luo Z, Pan J, Sun Y, Zhang S, Yang Y, Liu H, Li Y, Xu X, Sui Y, Wei S, Adv. Funct. Mater 2018, 28, 1804335b)Bencherif SA, Sands RW, Bhatta D, Arany P, Verbeke CS, Edwards DA, Mooney DJ, Proc. Natl. Acad. Sci. U.S.A 2012, 109, 19590. [PubMed: 23150549]

[9]. Zhang YS, Khademhosseini A, Science 2017, 356, eaaf3627. [PubMed: 28473537]

[10]. Bencherif SA, Warren Sands R, Ali OA, Li WA, Lewin SA, Braschler TM, Shih T-Y, Verbeke CS, Bhatta D, Dranoff G, Mooney DJ, Nat. Commun 2015, 6, 7556. [PubMed: 26265369]

[11]. Armstrong JP, Burke M, Carter BM, Davis SA, Perriman AW, Adv. Healthc. Mater 2016, 5, 1724. [PubMed: 27125336]

[12]. a)Stanton M, Samitier J, Sanchez S, Lab Chip 2015, 15, 3111 [PubMed: 26066320] b)Jungst T, Smolan W, Schacht K, Scheibel T, Groll J. r., Chem. Rev 2015, 116, 1496. [PubMed: 26492834]

[13]. a)Filardo G, Petretta M, Cavallo C, Roseti L, Durante S, Albisinni U, Grigolo B, Bone Joint Res. 2019, 8, 101 [PubMed: 30915216] b)Pi Q, Maharjan S, Yan X, Liu X, Singh B, van Genderen AM, Robledo-Padilla F, Parra-Saldivar R, Hu N, Jia W, Adv. Mater 2018, 30, 1706913.

[14]. Ying GL, Jiang N, Maharjan S, Yin YX, Chai RR, Cao X, Yang JZ, Miri AK, Hassan S, Zhang YS, Adv. Mater 2018, 30, 1805460.

[15]. Ying G, Jiang N, Yu C, Zhang YS, Bio-Des. Manufacturing 2018, 1, 215.

[16]. Peters EB, Christoforou N, Leong KW, Truskey GA, West JL, Cell. Mol. Bioeng 2016, 9, 38. [PubMed: 27042236]

[17]. Miri AK, Hosseinabadi HG, Cecen B, Hassan S, Zhang YS, Acta Biomater. 2018, 77, 38. [PubMed: 30126593]

[18]. Jungst T, Smolan W, Schacht K, Scheibel T, Groll J. r., Chem. Rev 2015, 116, 1496. [PubMed: 26492834]

[19]. Liu W, Heinrich MA, Zhou Y, Akpek A, Hu N, Liu X, Guan X, Zhong Z, Jin X, Khademhosseini A, Adv. Healthc. Mater 2017, 6, 1601451.

[20]. Porada CD, Zanjani ED, Almeida-Porada G, Curr. Stem Cell. Res 2006, 1, 365.

[21]. Satija NK, Singh VK, Verma YK, Gupta P, Sharma S, Afrin F, Sharma M, Sharma P, Tripathi R, Gurudutta G, J. Cell. Mol. Med 2009, 13, 4385. [PubMed: 19602034]

[22]. Zhang YS, Wang Y, Wang L, Wang Y, Cai X, Zhang C, Wang LV, Xia Y, Theranostics 2013, 3, 532. [PubMed: 23946820]

[23]. Wang Y, Ma M, Wang J, Zhang W, Lu W, Gao Y, Zhang B, Guo Y, Materials 2018, 11, 1345.

[24]. Shao N, Guo J, Guan Y, Zhang H, Li X, Chen X, Zhou D, Huang Y, Biomacromolecules 2018, 19, 3637. [PubMed: 30049206]

[25]. Yin Y, Xiao G, Zhang K, Ying G, Xu H, De Melo BA, Li S, Liu F, Yetisen AK, Jiang N, ACS Chem. Neurosci 2018, 10, 1411.

[26]. Gibbs DM, Black CR, Dawson JI, Oreffo RO, Tissue Eng J. Regen. Med 2016, 10, 187.

[27]. Pereira RF, Sousa A, Barrias CC, Bayat A, Granja PL, Bártolo PJ, Biomanufacturing Rev. 2017, 2, 1.

[28]. Ford MC, Bertram JP, Hynes SR, Michaud M, Li Q, Young M, Segal SS, Madri JA, Lavik EB, Proc. Natl. Acad. Sci. U.S.A 2006, 103, 2512. [PubMed: 16473951]

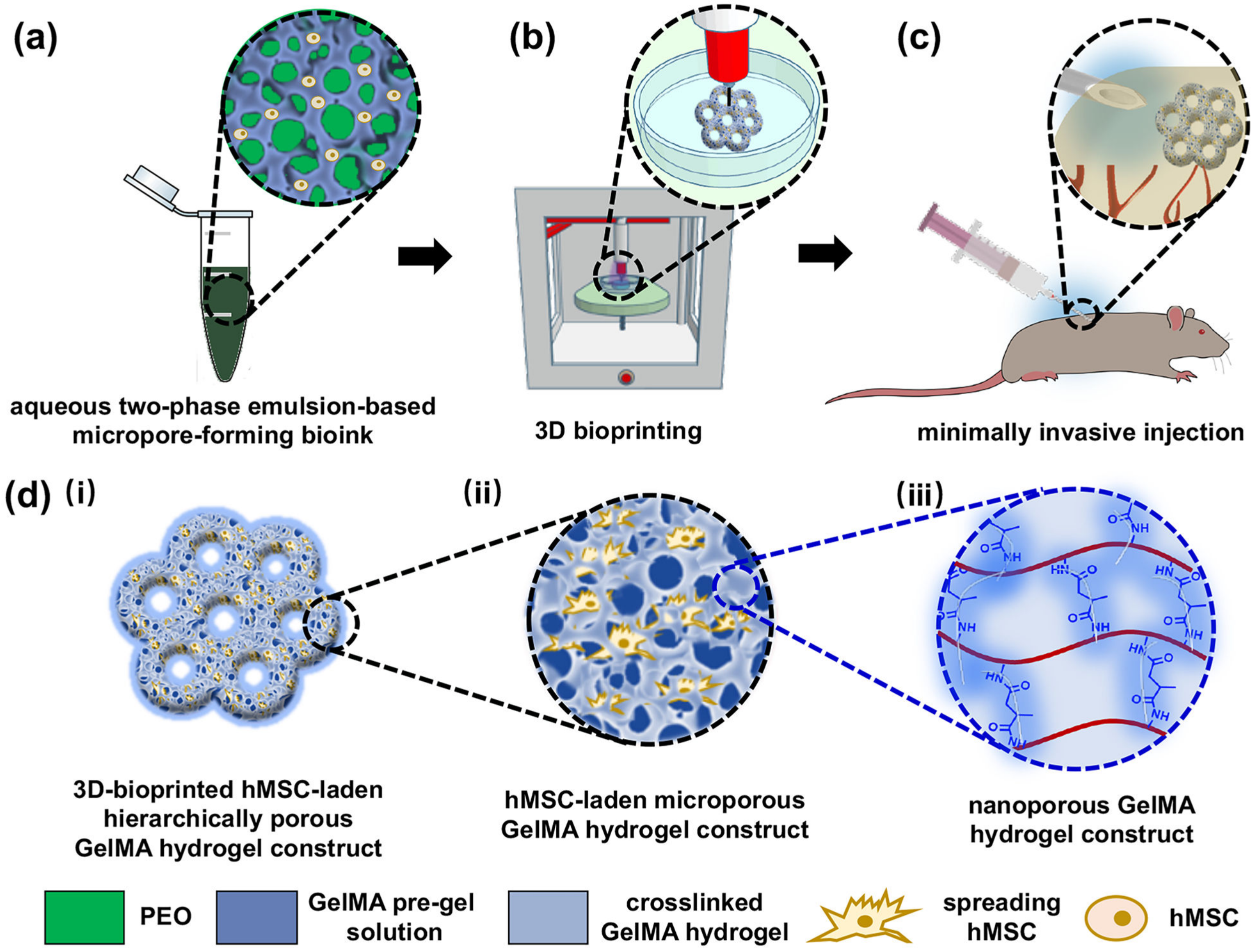

Figure 1.

Schematic showing the fabrication process of the 3D-bioprinted hierarchically porous hydrogel constructs by using an aqueous two-phase bioink. (a) The aqueous two-phase emulsion bioink containing the the pre-gel GelMA/cell and PEO blend. (b) 3D bioprinting and photocrosslinking. (c) Minimally invasive injection of the hierarchically porous hydrogel constructs. (d) The hierarchically macro-micro-nanoporous structure of the 3D-bioprinted GelMA hydrogel constructs: (i) macropores, (ii) interconnected micropores, and (iii) nanopores.

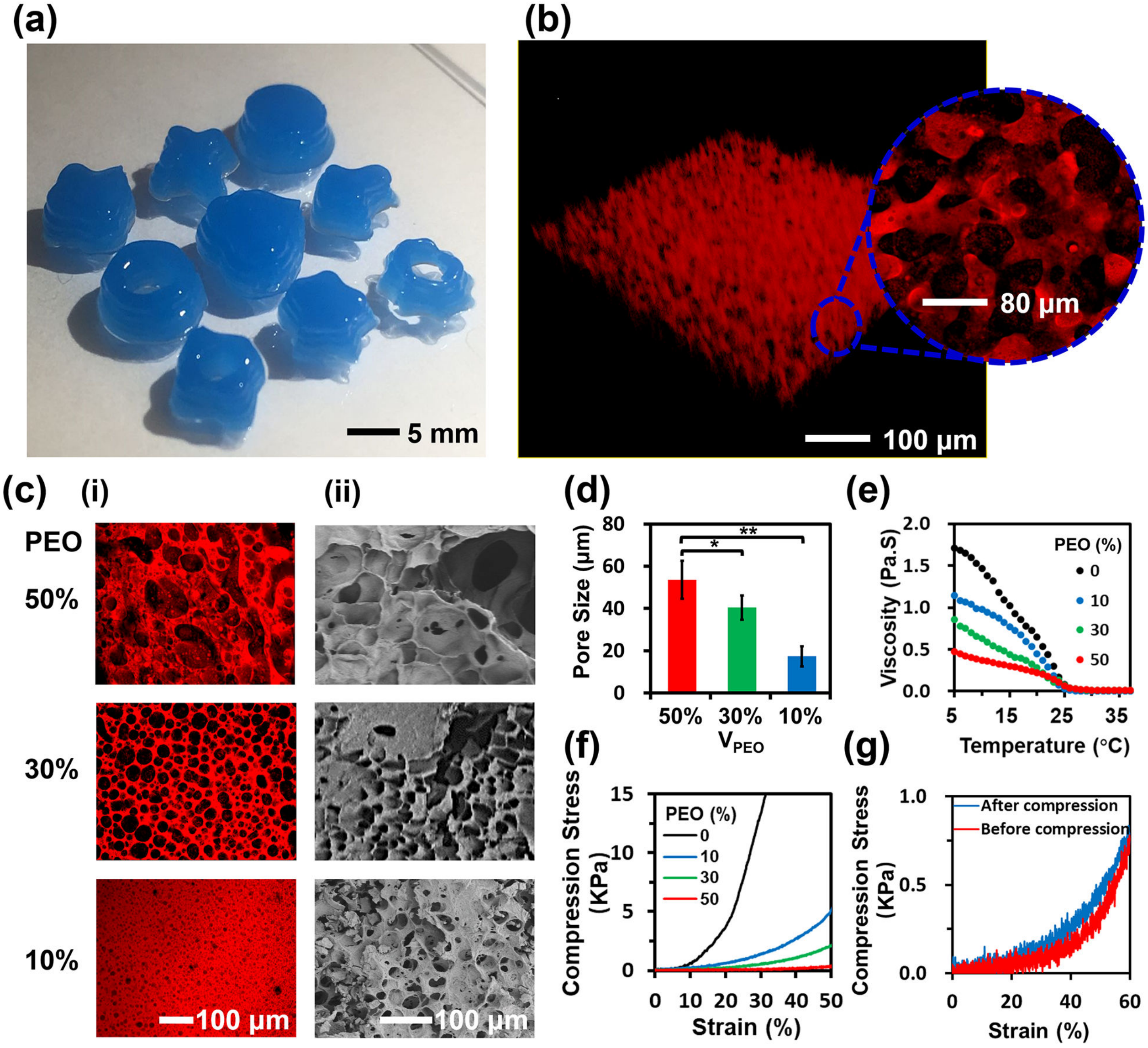

Figure 2.

Characterizations of the 3D-bioprintable hierarchically porous hydrogel constructs. (a) Photograph of 3D-bioprinted hydrogel constructs with different spatial shapes. (b) 3D reconstruction of a hierarchically porous hydrogel construct. Inset graph shows the magnified interconnected microporous structure. (c) (i) Fluorescence and (ii) SEM micrographs of the interconnected porous hydrogel constructs with PEO volume fractions at 10%, 30%, and 50%. (d) Average pore size variation of the hydrogel constructs as a function of PEO volume fractions at 10%, 30%, and 50% (n=3, $*p<0.05$). (e) Viscosity variation of the bioinks with PEO volume fractions from 0% to 50% as a function of temperature. (f, g) Stress-strain curves of the hydrogel constructs with (f) different PEO volume fractions, and (g) reversibility test (PEO=50 vol%).

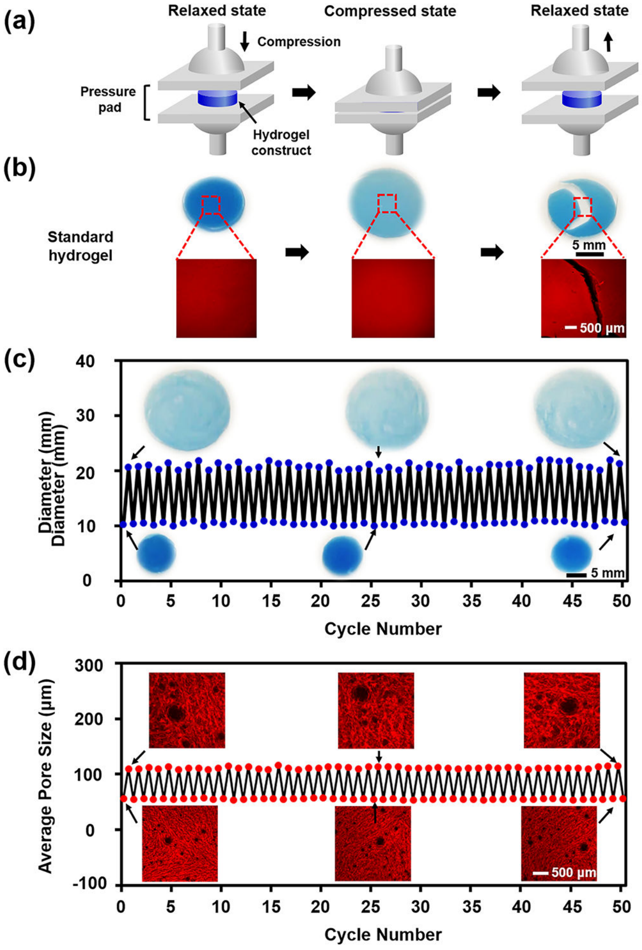

Figure 3.

Assessment of shape-memory property of the 3D-bioprintable micro-nanoporous hydrogel constructs. (a) Schematic of compression test procedure. (b) Morphologies and microstructures of the standard hydrogel constructs before (relaxed), during (compressed), and after (relaxed) compression test. (c) Diameter and (d) average pore size variations of the porous hydrogel constructs with 50 cycles of compression test. Insets shown in (c) are photographs and in (d) are fluorescence micrographs of the hydrogel constructs at the relaxed and compressed states after 1 cycle (left), 25 cycles (middle), and 50 cycles (right) of compression.

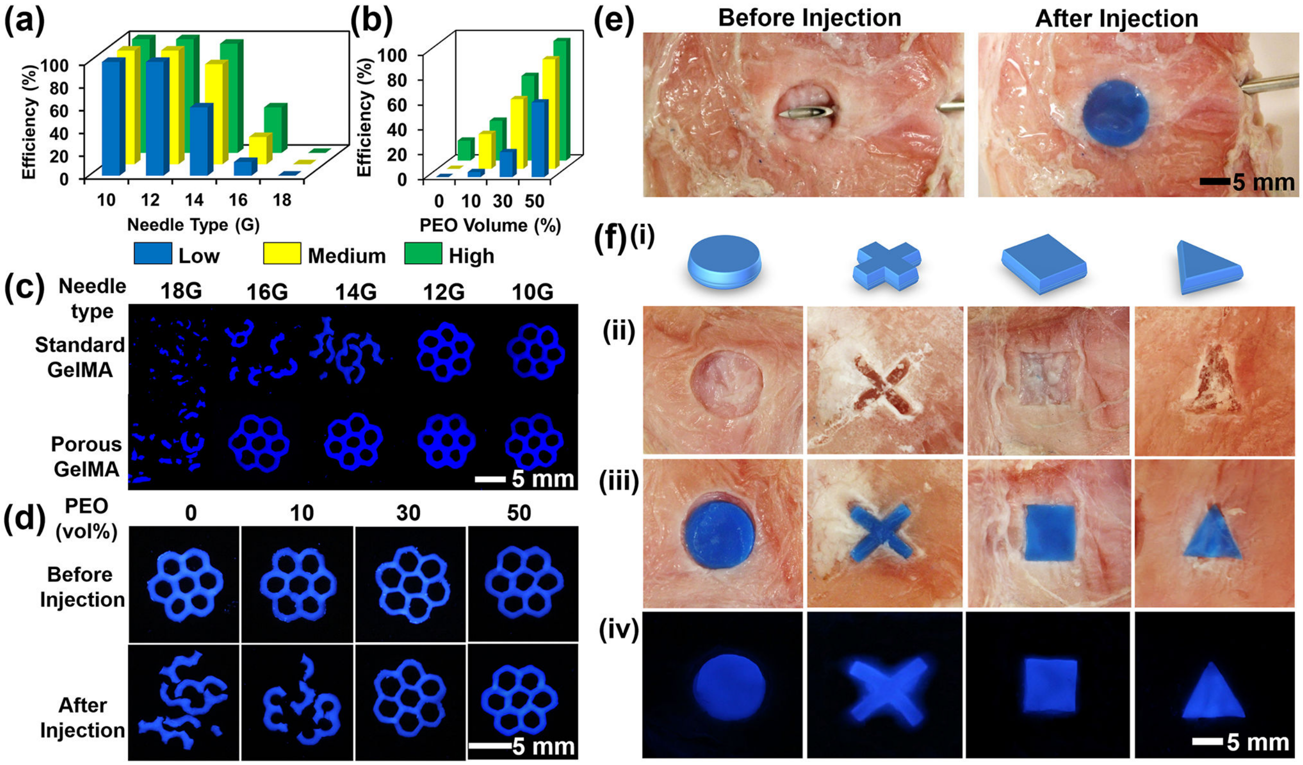

Figure 4.

Injectability tests of the 3D-bioprinted hierarchically macro-micro-nanoporous hydrogel constructs using various gauges of percutaneous needles *in vitro* and *ex vivo*. (a, b) Passage efficiency of the hydrogel constructs with different degrees of methacryloyl substitution (low, medium, and high) as a function of (a) percutaneous needle gauge and (b) PEO volume fraction. (c, d) Fluorescence micrographs of the 3D-bioprinted macro-micro-nanoporous hydrogel constructs (c) using various gauges of percutaneous needles after injection, and (d) at different PEO volume fractions before and after *in vitro* injection. (e) Photographs showing the injectability performances using a porcine tissue model. (f) Photographs of the shape-memory hydrogel constructs with different 3D patterns: (i) designs, (ii) porcine tissues cropped with different patterns, (iii) after injection of the hydrogel constructs within the corresponding porcine tissue defects, and (iv) fluorescence graphs of the hydrogel constructs within the corresponding porcine tissue defects.

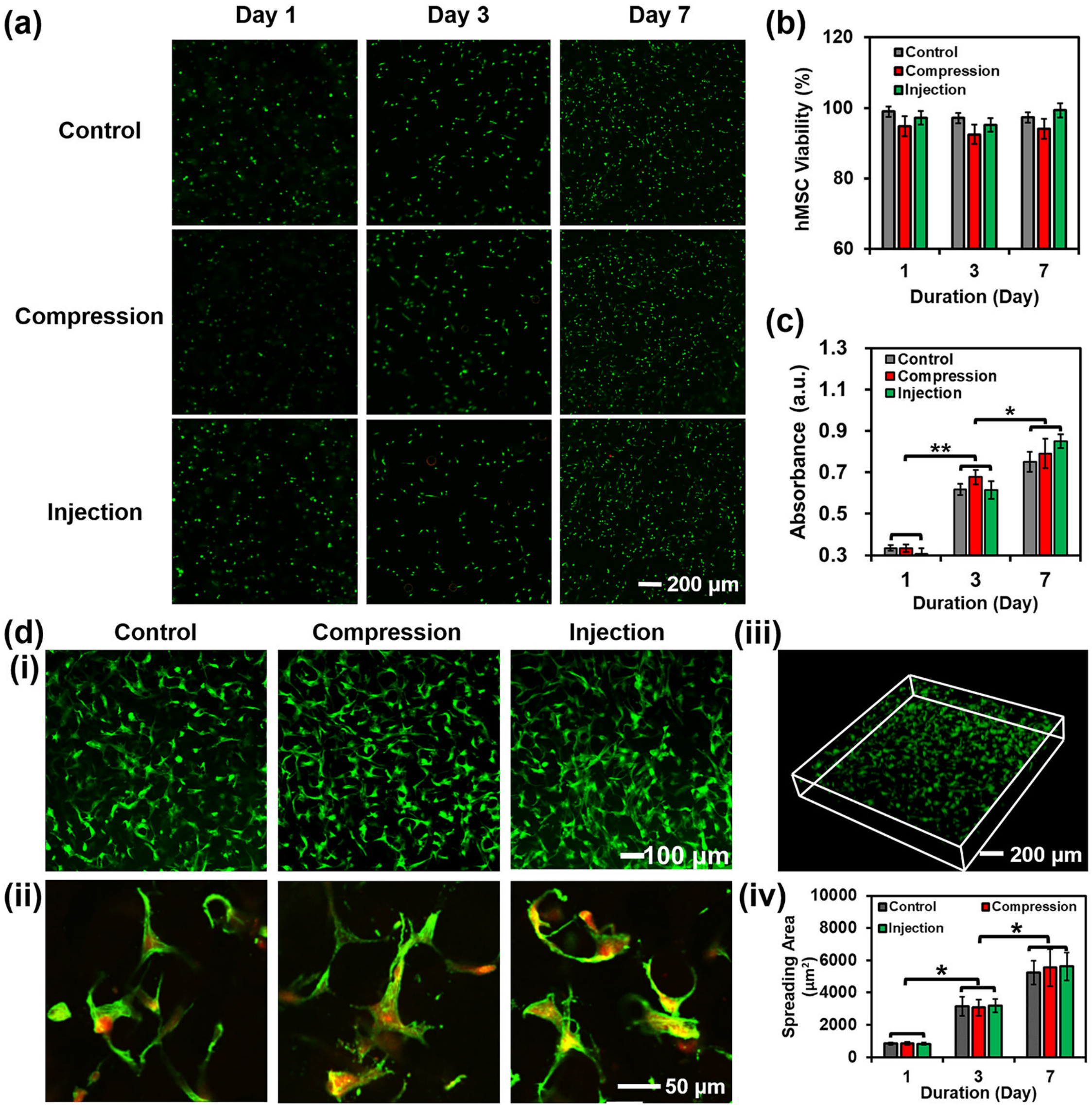

Figure 5.

Evaluation of hMSC viability and proliferation in the hydrogel constructs after compression and injection. (a) Fluorescence micrographs, (b) viability, and (c) proliferation of cells within the 3D-bioprinted porous hydrogel constructs before and after compression. Live cells were stained in green, while dead cells in red. The control group indicates the hydrogel constructs without compression and injection. (d) Fluorescence micrographs of cell spreading within the porous hydrogel constructs at (i) low and (ii) high magnifications. The cells were stained for F-actin (green) and nuclei (red). (iii) 3D reconstruction of spreading cells within a porous hydrogel construct. (iv) Calculated cell spreading areas on Day 1, Day 3, and Day 7 (n=3, *$p<0.05$).

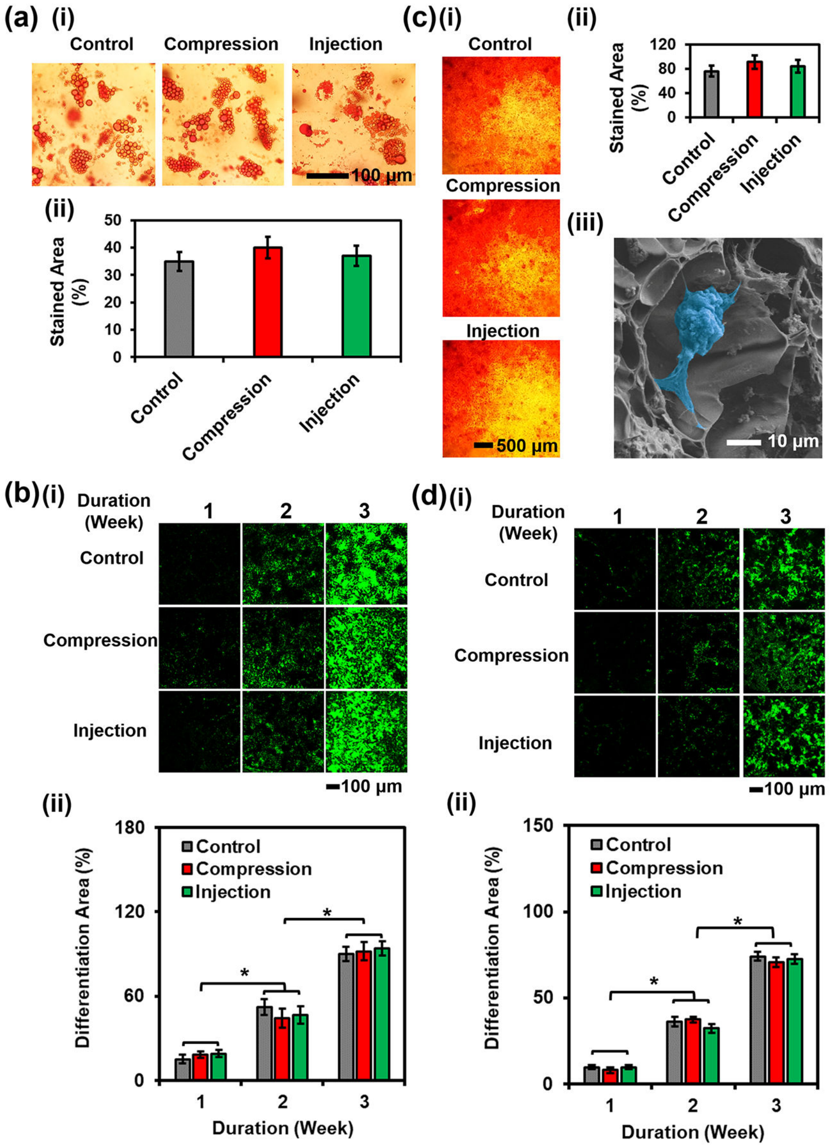

Figure 6.

Evaluation of hMSC differentiation within the 3D-bioprinted porous hydrogel constructs. (a) (i) Photographs and (ii) quantification of Oil Red O-stained hMSCs encapsulated in the 3D-bioprinted porous hydrogel constructs under different treatments at 3 weeks of adipogenesis. (b) (i) Fluorescence micrographs and (ii) semi-quantitative measurements of PPARγ immunostaining of hMSCs encapsulated in the 3D-bioprinted porous hydrogel constructs under different treatments over the course of 3 weeks of adipogenesis. (c) (i) Photographs and (ii) quantification of Alizarin Red S-stained hMSCs encapsulated in the 3D-bioprinted porous hydrogel constructs under different treatments at 3 weeks of osteogenesis. (iii) SEM micrograph of a differentiated cell (pseudo color in blue) and mineral deposition in the micro-nanoporous hydrogel at 3 weeks of osteogenesis. (d) (i) Fluorescence micrographs and (ii) semi-quantitative measurements of RUNX2 immunostaining of hMSCs encapsulated in the 3D-bioprinted porous hydrogel constructs under different treatments over the course of 3 weeks of osteogenesis (n=3, *p<0.05).

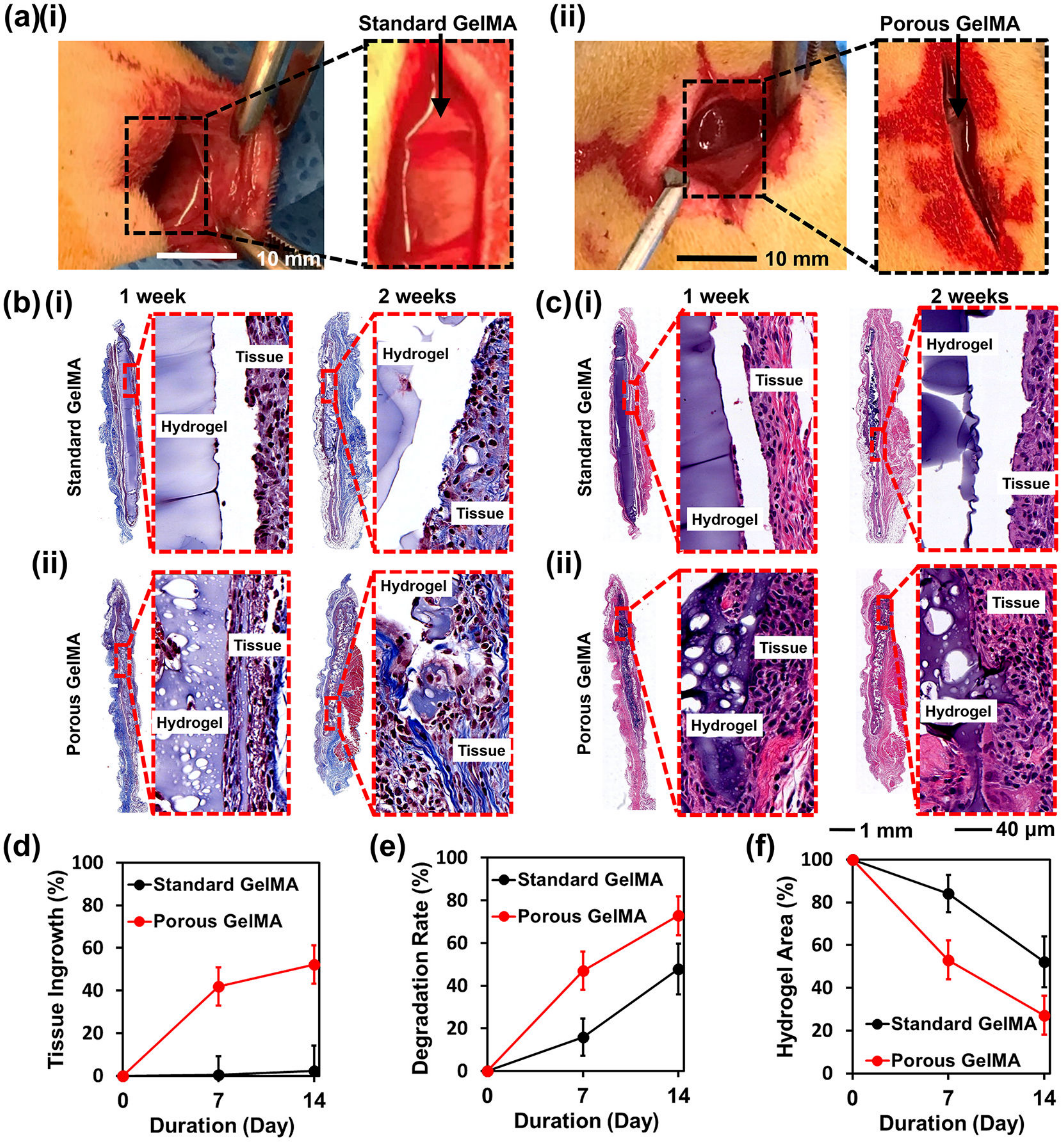

Figure 7.

In vivo study of the 3D-bioprinted hydrogel constructs. (a) Photographs of subcutaneous injection within rats. (b) Masson's trichrome staining and (c) H&E staining of (i) the standard GelMA hydrogel and (ii) the porous GelMA hydrogel at 1- week and 2- week post-implantation. (d) Tissue ingrowth rates as a function of implantation duration. (e) Hydrogel degradation rates within the tissue as a function of implantation duration. (f) Remained hydrogel areas within the tissues as a function of implantation duration (n=6).